ADVANCED INTELLIGENT SYSTEMS
Open Access
www.advintellsyst.com

3D Rotation-Trackable and Differentiable Micromachines with Dimer-Type Structures for Dynamic Bioanalysis

Gungun Lin,* Yuan Liu, Guan Huang, Yinghui Chen, Denys Makarov, Jun Lin, Zewei Quan, and Dayong Jin*

Utilizing the magnetic interactions between microparticle building blocks allows creating long-range ordered structures and constructing smart multifunctional systems at different scales. The elaborate control over the inter-particle magnetic coupling interaction is entailed to unlock new magnetoactuation functionalities. Herein, dimer-type microstructures consisting of a pair of magnetic emulsions with tailorable dimension and magnetic coupling strength are fabricated using a microfluidic emulsion-templated assembly approach. The magnetite nanoparticles dispersed in vinylbenzene monomers are partitioned into a pair of emulsions with conserved volume, which are wrapped by an aqueous hydrogel shell and finally polymerized to form discrete structures. Tunable synchronous–asynchronous rotation over 60 dB is unlocked in magnetic dimers, which is shown to be dependent on the magnetic moments induced. This leads to a new class of magnetic actuators for the parallelized assay of distinctive virus DNAs and the dynamic optical evaluation of 3D cell cultures. The work suggests a new perspective to design smart multifunctional microstructures and devices by exploring their natural variance in magnetic coupling.

1. Introduction

Bottom-up assembly of micro- and nanostructures is of general interest to construct functional materials and devices at different scales.[1–4] The assembly process can be driven by the spontaneous or directed organization of random building blocks to form ordered structures through localized interactions. Depending on the properties of the building elements, the assembled structures can be endowed with peculiar functions, enabling applications in sensors,[5] actuators,[6,7] photonics,[8,9] and electronics.[10,11]

Discrete magnetically actuated assembly structures[12–15] are preferred for non-tethered and contactless operations, flexible motility, and insensitivity to ambient environment, such as temperature, ionic strength, and conductivity, enabling applications in microactuators, motors, and robotic devices. The building blocks can include ferromagnetic,[14] diamagnetic,[16,17] or super/paramagnetic[18,19] micro- and nanostructures. Magnetic interactions exist between magnetic entities located in proximity. The interactions can transition from exchange[20] to dipolar-type coupling[21] at different length scales. Assembly of ferromagnetic particles has been relying on the magnetostatic interaction through the magnetic field emanating from the particles designed with specific morphologies and anisotropic properties.[14,21,22] On the other hand, magnetic dipole–dipole coupling is the driving force to guide the assembly of most paramagnetic or superparamagnetic particles. Most often, particles have been assembled

Dr. G. Lin, Y. Liu, G. Huang, Dr. Y. Chen, Prof. D. Jin
Institute for Biomedical Materials and Devices
Faculty of Science
The University of Technology Sydney
Ultimo, NSW 2007, Australia
E-mail: gungun.lin@uts.edu.au; dayong.jin@uts.edu.au

Dr. G. Lin, Y. Liu, Dr. Y. Chen, Prof. D. Jin
ARC Research Hub for Integrated Device for End-User Analysis at Low Levels
Faculty of Science
University of Technology Sydney
Sydney, NSW 2007, Australia

The ORCID identification number(s) for the author(s) of this article can be found under https://doi.org/10.1002/aisy.202000205.

DOI: 10.1002/aisy.202000205

Dr. D. Makarov
Helmholtz-Zentrum Dresden-Rossendorf e.V.
Institute of Ion Beam Physics and Materials Research
Bautzner Landstrasse 400, 01328 Dresden, Germany

Prof. J. Lin
State Key Laboratory of Rare Earth Resource Utilization
Changchun Institute of Applied Chemistry
Chinese Academy of Sciences
Changchun 130022, P. R. China

Prof. Z. Quan, Prof. D. Jin
UTS-SUStech Joint Research Centre for Biomedical Materials & Devices
Department of Biomedical Engineering
Southern University of Science and Technology
Shenzhen, China

into 1D to 3D arrays to deliver ensemble magnetoproperties,[4] including magnetochromatic[23–25] and magnetothermal effects. Limited approaches have been available to assemble a definite number of microparticles, which, nonetheless, is critical to control the inter-particle interactions. Chemical conjugation has been used to link a couple of magnetic microbeads to form discrete microswimmer structures,[26] but it has been difficult to decide the number of magnetic microbeads to be attached. Arrays of microparticles can be potentially patterned with precise inter-particle distance using microfabricated magnetic molds.[16,19] Nevertheless, the formation of discrete magnetic particle pairs and the elaborate engineering of the magnetic coupling thereof have not been addressed, as this typically requires the control over the size and encapsulated magnetic content of the particle building blocks.

Actuation-assisted bioanalysis represents an emerging application of micromachines, including microactuators, motors, and microrobotic devices. A range of external stimuli, such as heat,[27] light,[28–33] moisture,[34] chemical,[35,36] and magnetic field,[37–40] have been available to power the micromachines. For instance, light-driven mechanisms can enable local and site-specific actuation of a device. On the other hand, micromachines responding to humidity or chemicals are adaptive to the dynamic variations of chemical environments. Exploring such a variety of mobile micromachines in the bioanalytical field can further provide a range of benefits, including increased reaction binding kinetics, real-time, dynamic, and in situ measurements.[41–48] Beyond the precise control of a single microstructure, groups of microstructures are of utmost interest for applications that rely on collective behaviors, such as the dynamic sensing of toxins,[41–43] cleaning of environment pollutants,[44–47] and assembly of tissue scaffolds.[49] Large-scale and high-throughput biochemical analysis can benefit the most by parallelizing the assays using differentiable groups of stimuli-responsive microstructures, with each group allocated with a specific task. However, differentiation of microstructures using a single global control signal has proved challenging.[50] Furthermore, microstructures of biocompatible interfaces are ideal for handling small-scale tissues and tissue-like multicellular constructs that are often grown on 3D extracellular matrix. The dynamic analysis of the orientation-dependent features of such 3D structures remains a formidable task. Their tiny scale and opaque nature present major obstacles for both precise positioning and high-quality microscopy evaluation.[51]

Here, micrometer-sized magnetic emulsions are artfully assembled in polymer gels to achieve tailorable magnetic coupling in magnetoresponsive dimer-type assemblies. Based on a rationally designed emulsion polymerization process in microfluidics, multicompartment microstructures are constructed by partitioning magnetic nanoparticles into a pair of micrometer-sized emulsions with conserved total volume. They are subsequently assembled and finally immobilized with a high level of structural order. The coupling between the emulsion compartments unlocks new degrees of freedom to elaborately engineer magnetic anisotropy within the structures. This leads to the design of 3D rotation-adaptive microactuators that can be manipulated and differentiated using a single global control signal, thereby closing the gap for dynamic bioanalysis, such as the precise positioning and optical evaluation of 3D multicellular structures and parallelized screening of multiple distinctive pathogenic virus DNAs in a single test.

2. Results and Discussion

2.1. Emulsion-Templated Assembly of Magnetic Microstructures with Tailorable Inter-Particle Coupling

To tailor the interaction between the magnetic building blocks, we put forth a compartmentalization-assembly strategy (**Figure 1**) to synthesize dimer-type structures consisting of two magnetic particle compartments. Compartmentalization refers to encapsulating magnetic nanocores, in isolated micrometer-sized emulsions. The total energy of the dimer system can be approximated by

$$E = -(\vec{m}_1 + \vec{m}_2) \cdot \mu_0 \vec{H} + \frac{\mu_0}{4\pi}\frac{1}{L^3}\left[\vec{m}_1 \cdot \vec{m}_2 - 3(\vec{m}_1 \cdot \hat{r})(\vec{m}_2 \cdot \hat{r})\right] \quad (1)$$

with the first term describing the Zeeman energy, and the latter the dipole coupling energy. Here, L is the distance between the dipoles, m_1 and m_2 are the moments of each dipole entity, and μ_0 is the magnetic permeability. Here, individual magnetic building blocks with definite sizes, e.g., r_1 and r_2, are approximated as interacting dipoles. Anisotropy is induced by the dipolar coupling and control over the geometric factors, such as L, r_1, and r_2, thus opening a window to investigate the interaction in a more systematic manner. This involves the way the assembled microstructures respond to external magnetic stimuli (Figure 1b). Exploring the variance in coupling between the magnetic building blocks may endow the resultant microstructures with built-in differential response (Figure 1c) without turning to external addressable actuation.

To assemble the structures, a two-step microfluidic emulsification process was implemented using microcapillaries co-axially aligned and connected with two flow junctions (**Figure 2**a and Figure S1, Supporting Information). The rapid re-circulation in emulsion droplets is ideal for homogeneously dispersing nanoparticles in polymers.[52,53] Based on such design, the number (N) of the compartments can be regulated by the ratio of the emulsification frequencies (ν_1 and ν_2) at different steps[54,55]

$$N = \frac{\nu_1}{\nu_2} = \left(\frac{Q_1}{Q_1+Q_2}\right)\left(\frac{D_3}{D_2}\right)^3\left(\frac{a_2(Q_1+Q_2)/Q_3+b_2}{a_1(Q_1/Q_2)+b_1}\right)^3 \quad (2)$$

Here, Q_1, Q_2, and Q_3 are the flow rates of the inner, middle, and outer fluid phases, respectively; a_1, a_2, b_1, and b_2 are all constants determined by the dimension of the fluidic junctions. As the multiphase emulsification is purely mediated by the flow rate without any other free parameters, distinct multicompartment core–shell structures can be generated on demand.

To be noted, the above-mentioned dependency typically applies for general scenarios when N is well above 1.[55] It is shown that by bringing the emulsification frequency ratio (N) below 1, a typical unexplored regime, the frequency ratio reflects the size ratio of internal compartments (Figure 2b). This provides a new approach to fine tailor the above-mentioned geometric

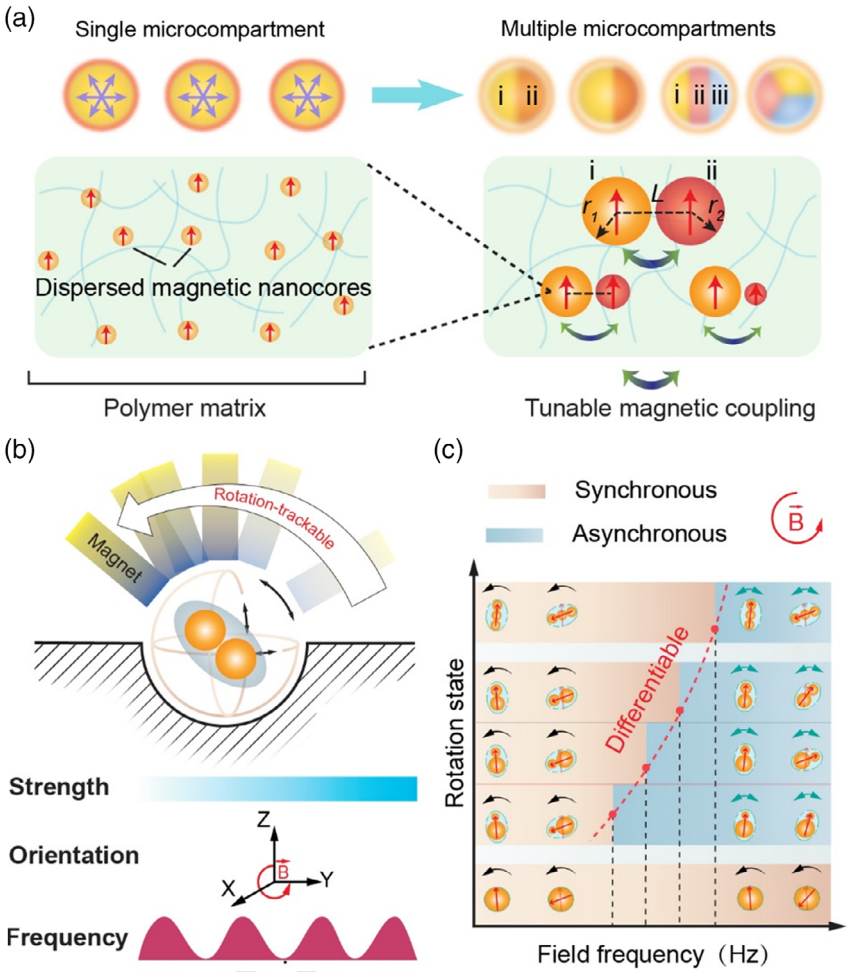

Figure 1. Engineering magnetic coupling in microstructure assemblies consisting of multiple magnetic compartments. a) Conceptual illustration of the approach to distribute active magnetic nanocores in a polymer matrix. (Left) Single compartment of magnetic nanocores that are dispersed in the polymer matrix. (Right) Controlled organization of individual microcompartments (denoted by i–iii) to form long-range structural order, which allows tailoring the magnetic interactions between the compartments. Here, r_1, r_2, and L denote the size of each compartment and spacing thereof, respectively. The red arrow denotes the magnetic moment. Gaining control over the above-mentioned parameters virtually allows engineering magnetic coupling thereof. b) Multicompartment microstructures can be tracked using a rotating magnetic field (B) with definite strength, orientation, and frequency. c) Groups of multicompartment structures can be differentiated based on their rotation states, namely, how they perceive and interact with the magnetic control source. Fully magnetically isotropic micromachines exhibit only synchronous rotation that are not different in the way they respond to a rotating magnetic stimulation. In contrast, multicompartment microstructures with elaborately engineered magnetic anisotropy exhibit differentiable asynchronous rotation.

parameters based on the emulsion fission. To facilitate this process, elaborate control over the flow rates was implemented to ensure that emulsions generated at the first junction break up well before they pass through the second junction. The resultant dimer structures are of unique pear shapes, as presented in Figure 2c. The total volume of the magnetic compartments is conserved for a series of dual-compartment structures as they are generated by the fission of one parental emulsion compartment. Systematic adjustment of the relative portion of magnetic compositions, hence, becomes possible. To explore the major flow regimes, the careful control of the flow parameters, namely, the Q_1/Q_2 and $Q_3/(Q_1+Q_2)$, reveals four major distinct structural patterns such as those shown in Figure 2c. Their size can be ranging from 50 to 500 μm, depending on the diameter of the fluidic orifice and specific flow rates chosen. Among these patterns, two are stable and characteristic, representing both digital and analogue modulation of magnetic compartments: one comprising uniform compartments, and the other resembling pears, with N experimentally tunable from 0.5 to 6.

Based on the controlled emulsification process, polymerization techniques were next used to construct multicompartment magnetic assemblies. Ferrofluid magnetite particles (SPIONs) with a nominal size of 10 nm were used as the magnetic nanocores. The SPIONs were blended with oily divinylbenzene (DVB) and emulsified into an aqueous solution using a microfluidic flow-focusing junction. Figure 2d shows two critical steps to synthesize the magnetic structures with polymer shells and desired compartmental layout (details are given in

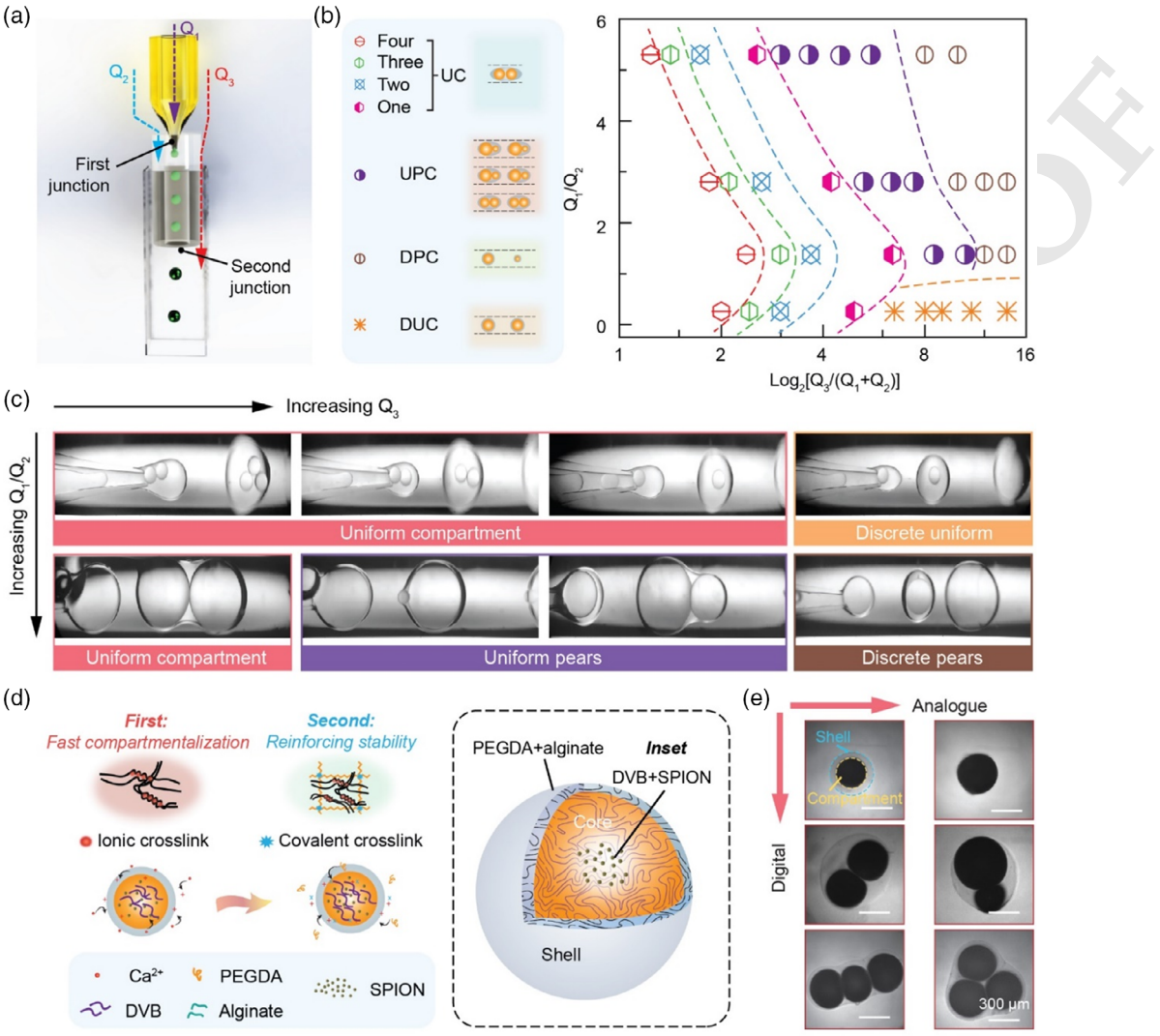

Figure 2. Construction of multicompartment magnetic structures using microfluidic emulsion-templated assembly. a) Schematic illustration of a microfluidic setup to synthesize the multicompartment magnetic structures. The setup is consisting of microcapillaries connected by two flow junctions. The first junction is to generate emulsion compartments, and the second junction is used to form a shell that encloses the compartments in discrete entities. Q_1, Q_2, and Q_3 are the flow rates of inner, middle, and outer fluidic phases, respectively. b) Representative regimes of fabricating multicompartment double emulsion structures of different levels of structural order. UC: uniform compartments; UPC: uniform pear-shaped compartments; DPC: discrete pear-shaped compartments; and DUC: discrete uniform compartments. c) Images of distinct ordered structures formed in the channel consisting of uniform emulsion compartments, pear-shaped structures with uneven compartments, and non-uniform structures with single compartments. Q_1, Q_2 and Q_3 are the same as (a). d) Two processing steps are involved: Step 1 is to form in situ the alginate shell by adding Ca^{2+} to generate ionic crosslinks, and Step 2 is to form covalent bonds in the polymer shell by UV illumination to generate covalent crosslinks. (Inset) Compartment (core)–shell composition of the structures. e) Microscopy images of representative magnetic microstructures with digital modulation embodied by varied compartment number, or analogue modulation embodied by tailored volume-compartment ratio, compartment-size ratio, and compartment layout. Scale bar for all images in (e): 300 μm.

Experimental Section). In brief, to quickly immobilize the ordered compartments, alginate hydrogel polymers were first applied as the encapsulation layer of the emulsion compartments, formed during the second emulsification step at the second junction. By introducing Ca^{2+} ions in the outer oil phase, the alginate shell was rapidly crosslinked to protect the highly volatile magnetic emulsion compartments from coalescence. In addition to the ionic crosslinking mechanism, covalent crosslinking was next implemented to reinforce the stability of the alginate layer. For this, the preformed structures were collected in a bath containing aqueous poly(ethylene glycol) diacrylate (PEGDA) precursors, which were introduced in the alginate matrix by diffusion through the pores of alginate polymers. This processing step strengthened the shell by forming stronger covalent bonds under UV exposure. The final microstructures consisting of varied compartment and biocompatible hydrogel shell interfaces are shown in Figure 2e.

2.2. Exploring Synchronous–Asynchronous Rotation Transition by Engineering Dipolar Coupling

To study the rotation response, magnetic dimer-type structure assemblies were suspended in water and subject to rotation under an external rotating magnetic field with adjustable strength and frequencies (**Figure 3**a). The critical rotation state is defined as a threshold point when a structure transitions from *synchronous* rotation when it can still follow the pace of the rotating field to *asynchronous* rotation when it no longer does and simply wiggles (Figure 3b). A sudden drop of the rotating frequency of the structure was observed at the critical state when the external field frequency is gradually increased from 0 to 25 Hz (Figure 3c). Upon that case, the rotation curves manifest themselves as an additional oscillation superimposed on the linearly growing curves. The oscillation of the curves tells that the structures rotate backward as opposed to the rotating direction of the magnetic field. Such a backward movement, as termed "wiggling," is due to the fact that the angle ($\Delta\theta$) between the direction of the magnetization of the structures and that of

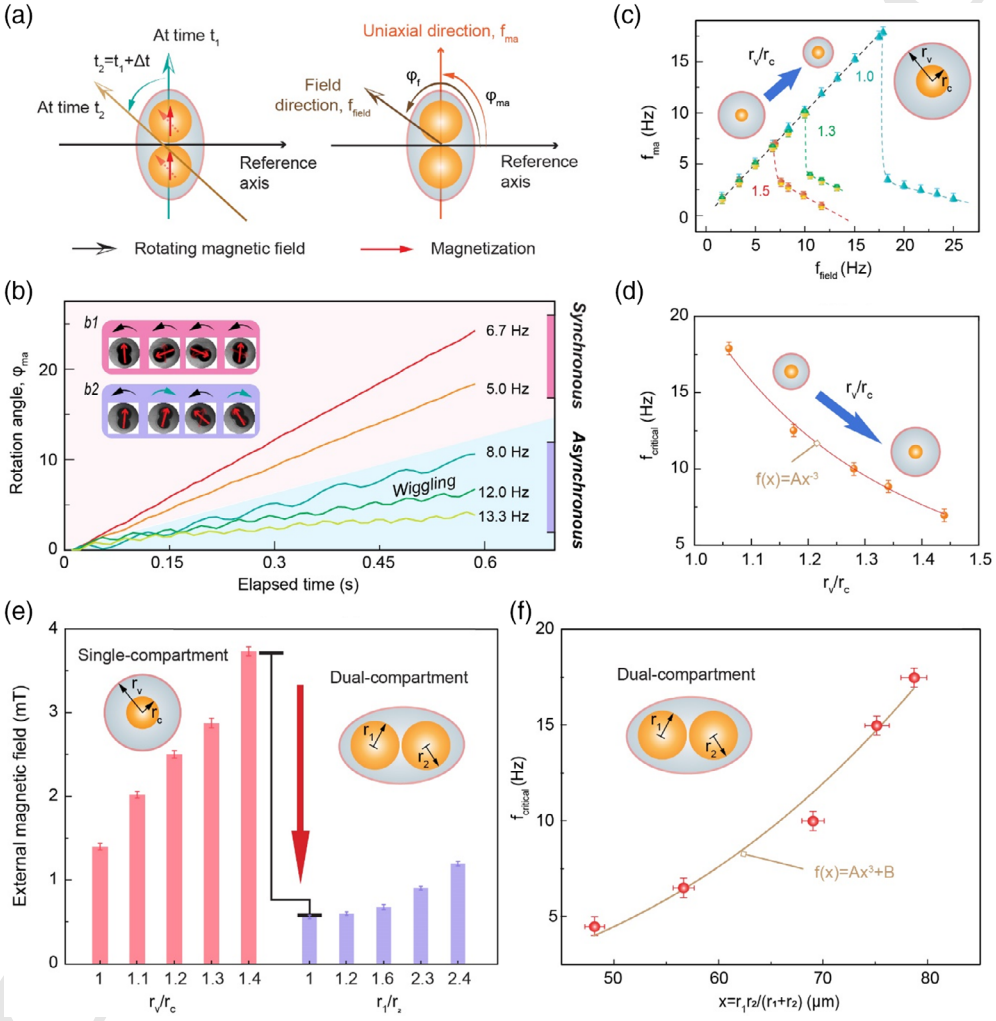

Figure 3. Exploring synchronous–asynchronous rotation transition using a rotating magnetic field. a) Schematic illustration of characterizing a dual-compartment magnetic dimer-type structure using a rotating magnetic field. The directions of the magnetic field at different time, e.g., t_1 and $t_2 = t_1 + \Delta t$, are indicated by the arrows. The compartment-to-compartment direction of the structure corresponds to the uniaxial direction of the structure. The rotation angles of the field and the structure with respect to the reference axis are denoted by φ_f and φ_{ma}, respectively. Accordingly, the frequencies of the field and the structure are denoted by f_{field} and f_{ma}, respectively. b) Time-dependent rotation angle, φ_{ma}, of a structure driven by a magnetic field (1 mT) at different rotation field frequencies. Inset shows the time-sequenced images of the structure in synchronous (b1) and asynchronous (b2) rotation states. Arrows show the uniaxial direction of the structure. c) Dependence of the rotation frequency of single-compartment structures with different volume-compartment ratios under the same rotating magnetic field of 2.5 mT at different rotating frequencies. d) Plot of the critical frequencies ($f_{critical}$) of the single-compartment structures against the volume-compartment ratio. Line is a fit to the data. e) Dependence of the required magnetic field strength to rotating different micromachine structures to the same critical frequency of 10 Hz. There is a significant drop of magnetic field strength needed for dual-compartment structures, despite that they contain the same amounts of magnetic content as the single-compartment ones with volume-compartment ratio of 1.4. f) Plot of the critical rotation frequency ($f_{critical}$) against the geometric factor, $r_1r_2/(r_1 + r_2)$ of dual-compartment structures. The solid line is a fit of the data using the polynomial function displayed in the figure. Error bars in all plots represent the accuracy of the measured quantities.

the magnetic field reaches 90°. With increasing driving frequency of the field, the time taken for $\Delta\theta$ to reach 90° is proportionally reduced. This accounts for the scaling of the oscillation frequency with the driving frequency of the field.

For idealized superparamagnetic microspheres with purely induced magnetic moment, there is no explicit dependence of the rotating frequency of the structures on the external driving field at low frequencies.[56] However, the apparent dependency of the critical rotation frequency (f_{critical}) on the driving field (f_{field}) and on the size ratio of the magnetic compartment, as shown in Figure 3c, suggests the existence of mesoscopic "permanent moments." In this regard, the "permanent moments" refer to "part of the materials in the structures that do not instantaneously align its magnetic moment with the field as permanent at the time scale of experiments" in previous studies.[57] In the case that structures driven mainly by permanent moments, its critical rotating frequency is obtained by balancing the hydrodynamic torque and magnetic torque[58]

$$f_{\text{critical}} = \frac{\mu_0 \pi m H}{3\eta V} \tag{3}$$

where μ_0 is the magnetic permeability, m is the magnetic moment, H is the magnetic field, η is the dynamic viscosity, and V is the total volume of the rotating body. This relationship suggests a cubic law dependence of the critical frequency on the size ratio between the compartment and the total volume, which is reflected in Figure 3d. This result further confirms that the major magnetic driving force comes from the minor permanent moment for the class of single-compartment structures.

Figure 3e compares a series of single- and dual-compartment dimer-type structures. It is shown that by introducing additional compartments to the structures, the magnetic torque is enhanced, and the magnetic field to drive the structures to the same critical rotating frequency of 10 Hz can be reduced by threefold. Based on Equation (1) and details of the derivation provided in Supplementary Section 1, Supporting Information, the rotation frequency of the dimer-type structures can be estimated using the relationship as follows

$$f_{\text{ma}} = 2\pi(\omega^{\text{i}}{}_{\text{critical}} \sin 2\theta + \omega^{\text{p}}{}_{\text{critical}} \cos\theta) \tag{4}$$

We define θ as the phase lag between the structure and the field, and $\omega^{\text{i}}{}_{\text{critical}}$ and $\omega^{\text{p}}{}_{\text{critical}}$ are the critical angular frequencies of induced and permanent moments, respectively. The validity of the above-mentioned relationship was confirmed by applying the structure as a viscometer (Figure S2, Supporting Information). In this regard, the viscosity of water at different temperatures as well as that of the aqueous glycerol solutions with different concentrations have been successfully determined using the critical rotation frequency of the microstructures.

We realize that the relative contributions of the induced or permanent moments can have a strong influence on the critical frequency, which can be either tuned or independent on the structural modulation. In the former case, the critical frequency of the structure can be approximated as

$$f_{\text{critical}} = 2\pi(\omega^{\text{i}}{}_{\text{critical}} + 0.7\omega^{\text{p}}{}_{\text{critical}}) \tag{5}$$

To understand the relative roles of permanent and induced moments, the dependence of the critical frequency is plotted against the geometric factor defined by $r_1 r_2/(r_1 + r_2)$, where r_1 and r_2 are the size of the compartments (Figure 3f). Fitting the above-mentioned data to the relationship described in Equation (5) yields the magnetic susceptibility of the structures (≈9.1) that is consistent with the provided value (18.6) of the ferrofluids (EMG 900) with a volume fraction of 50%. This result indicates that tuning the synchronous-to-asynchronous transition states of the unconventional class of dual-compartment microstructures relies on induced magnetic moments, which is in stark contrast with that of single-compartment ones. It can be further concluded that the rotation transition states resulting from magnetic dipole–dipole coupling can be effectively tuned through the structural modulation of magnetic building blocks with primary contribution from induced magnetic moments. Remarkably, the unlocked tunability in the characteristic critical rotation frequency, found in dual-compartment microstructures, can be spanning over 60 dB owing to the enhanced magnetic field-structure interactions (Supplementary Section 1, Supporting Information).

2.3. Multiaxial Positioning of 3D Multicellular Constructs for Evaluation

The dipole–dipole coupling-induced magnetic anisotropy of dimer-type structures opens the possibility to design functional actuation tools for complex cellular analysis. The magnetic dimer-type structures were applied as 3D extracellular matrix of multicellular constructs. To facilitate the operation, a compact device was fabricated by inserting a permanent magnet into a 3D-printed slide rail with a footprint of 3 cm × 3 cm × 1.5 cm, as shown in **Figure 4**a. It is shown that the structure can be compassed precisely by the magnet (Figure 4b, and Video 2, Supporting Information). In this way, the rotation of the 3D extracellular matrix embodied by the dual-compartment structures can be tracked by the position of the magnet, which is further used to index the orientation of the 3D cell cultures grown on the hydrogel-based extracellular matrix.

The cells were seeded in agarose wells where the structures were suspended. The agarose wells were casted from a mold fabricated by 3D printing (Figure 4c). The hydrogel surface of the assembly structures can facilitate cell adhesion and growth. The hydrogel shell of the assembly structures was coated with positively charged poly-Lysine to further enhance the adhesions of the negatively charged cells[59] and to form 3D cultures. While a confocal microscope only provides single-axis details of the cells, using the structures with 3D rotational degrees of freedom, it is shown that the distribution of cells on the side and bottom of the entire spheroid was revealed (Figure 4d). In 3D multicellular constructs, cells were distributed around the entire 3D extracellular matrix. In bright-field imaging, cells were hidden above the dark background of the magnetic components (**Figure 5**a). We find that by expanding the ratio between the extracellular matrix and the assembly, the hidden cells were revealed by rotating or inclining the imaging planes, as shown in Figure 5b,c.

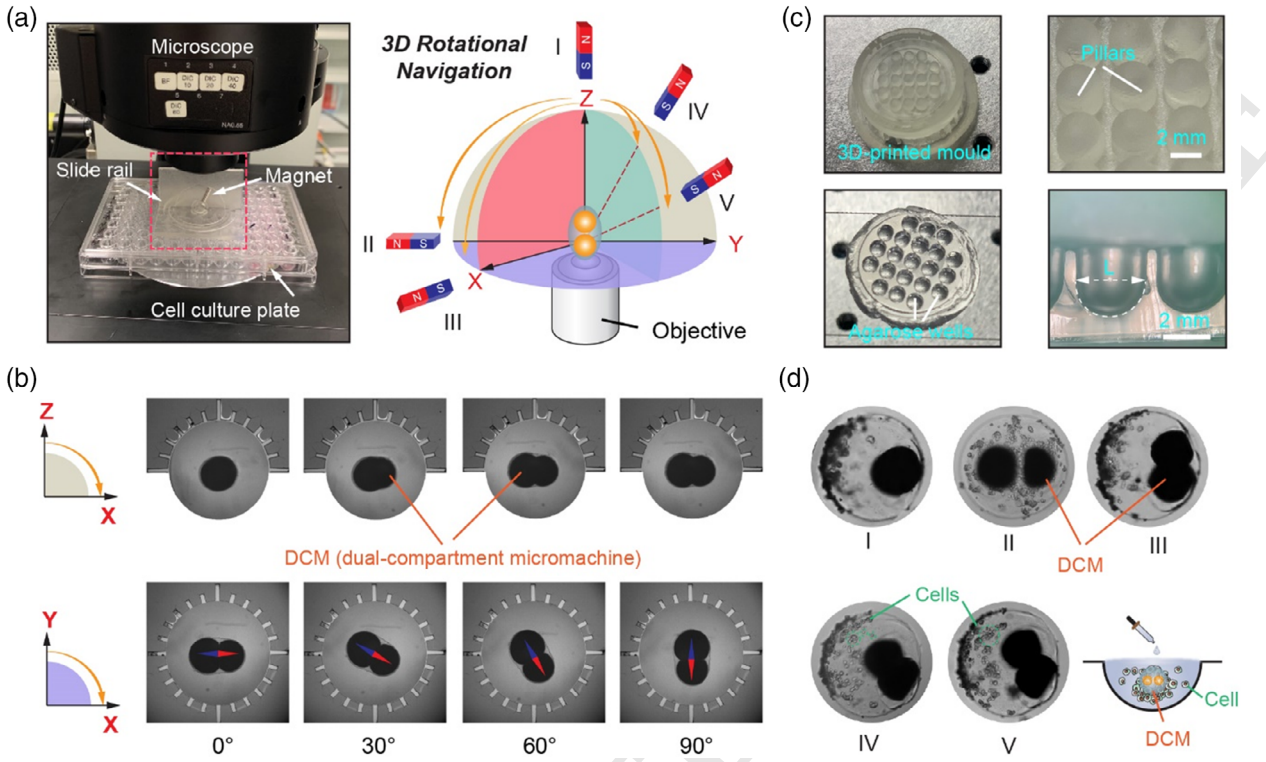

Figure 4. Magnetic tweezing system for the 3D rotational navigation. a) Design and assembly of compact slide rails with a movable permanent magnet, which is implemented in a light microscope to image cell cultures in a microwell plate. 3D rotational degree of freedom can be achieved to control the orientation of hydrogel tweezers using the magnet. b) Projection images of the dual-compartment structures (DCM) on the *x*–*z* and *x*–*y* planes being oriented along arbitrary directions. c) Photograph of 3D-printed wells with arrays of millimeter pillars (top row) to cast agarose culture wells with different sizes (bottom row). d) Microscopy images of cells grown on 3D extracellular matrix on the micromachine structures, which are manipulated by the magnet and viewed from different facets. Images (I–V) correspond to the positions marked in (a). The bottom right corner is the illustration of seeding and growing cells on the micromachine structures.

To expand the matrix, the structures were soaked in a culture medium depleted with Ca^{2+}. This controllably expands the size of the alginate-based extracellular matrix by swelling. On the other hand, in the most case of using fluorescent labels to stain the cells, where the above-mentioned dark contrast-related issues could ~~become~~ circumvented.

In this study, without innovating the imaging algorithm that aims to reduce noises and separate cell clusters, a basic demonstration of analyzing cell distributions in 3D was conducted using the rotation-trackable structures. Cells were recognized using Image J as colored spots (Figure 5d). As the cells are distributed around a well-defined sphere, the cell positions extracted from a 2D imaging plane (*x*–*y*) can be translated into coordinates in other planes using rotation matrices ~~using~~ mathematical calculations (Supplementary Section 4, Supporting Information). With this capability to image on different planes, the cell culture conditions were evaluated. For instance, cells were previously found to have different growing tendencies on the sedimentation flux densities of seeding cells.[60,61] It was revealed that the effects limit the seeding cells to either self-aggregate or adheres on the 3D extracellular matrix (Figure 5f,g) ~~that~~ can be evaluated by the rotational-trackable structures.

2.4. Parallelized Analysis of Distinctive Biomolecular Analytes

The tunability and distinguishability in the rotational actuation of magnetic assembly structures will further meet the need for the dynamic screening of multiple distinctive biomolecular analytes,[62] such as viral oligo species. As the differentiable critical rotation frequencies, as the rotational signature, can be fine-tuned on demand using the variance in the dipole–dipole coupling strength built into the structures, an unconventional collection of responsive magnetic microcarriers is established to simultaneously detect an array of target pathogenic DNAs using a microfabricated fluidic chip (**Figure 6**a).

Here, five batches of rotation-differentiable structures exhibiting five unique critical rotation frequencies were synthesized, ranging from 2 to 19 Hz with deviation of the frequencies within ±0.5 Hz. Different batches of structures were functionalized with different types of single-strand capture DNAs, targeting DNAs including that of Ebola virus (EV), human immunodeficiency virus (HIV), human papillomavirus (HPV), hepatitis C virus (HCV), and hepatitis B virus (HBV). The testing sample contained two positive species of HCV and HBV target DNA molecules. In the proof of the principle experiment, as shown in Figure 6b, a microchip containing 10 × 10 fabricated wells

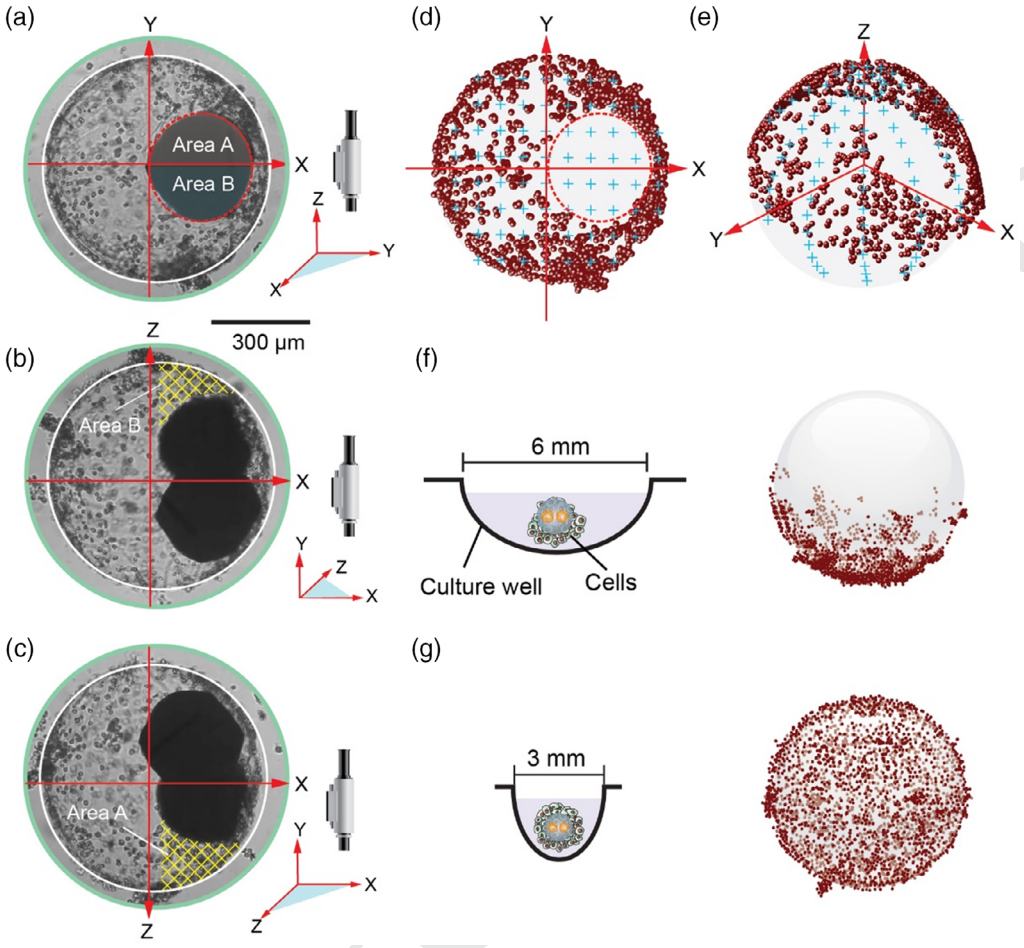

Q6 **Figure 5.** Multiaxial optical analysis of 3D cell cultures enabled by rotation-trackable structures. a–c) Multiaxial view (grayscale images) of 3D cell cultures grown on structures with purposely expanded extracellular matrix. The white ~~dashed~~ circle indicates the outer rim of the extracellular matrix. The red dashed circle marks the magnetic compartment. The cells shielded by the dark contrast of the micromachine in (a) are revealed by rotating the 3D cell cultures that are imaged on the *x*–*z* plane, as shown in (b,c). d,e) 2D and 3D distributions of cells, respectively. Here, a cell is denoted by a dot, the distribution of which is extracted from the initial greyscale image shown in (a) using an image processing program. f,g) Analyzing cell distributions under different culture conditions using culture wells of f) 6 mm and g) 3 mm diameters.

was used to entrap structures for the differentiable reading. By sweeping the rotation frequency of the magnetic field from 1 to ~~35~~ Hz, as the results shown in Figure 6c, the critical frequencies of each micromachine can be well identified, so that the target DNAs species can be detected simultaneously in a single test.

3. Conclusion

In this article, we have demonstrated a new emulsion partitioning approach to engineer the inter-particle coupling in basic dimer-type assembly structures. A collection of microstructures consisting of magnetic emulsion compartments embedded in polymers has been assembled with the assistance of microfluidics due to its superior control over individual emulsions in a continuous flow process. The emulsion partitioning approach allows allocating the magnetic content between the compartments of the dimer structures. The assembly of the magnetic compartments unlocks new degrees of freedom to modulate dipole–dipole coupling through the tunable compartmental size and size ratio. We have found that the synchronous–asynchronous rotation transition relies primarily on the magnetic moment induced for the dimer structures, rather than on the permanent ones inheriting from the original magnetic nanocores for single-compartment ones. This shine[illegible]ght on the roles of different types of magnetic moments in ~~the~~ actuating engineered magnetic structures using a magnetic field. The unique dimer-type emulsion assembly with tunable coupling strength leads to an unconventional class of magnetic actuators, of potential use in complex and dynamic bioanalysis. While it has been known that magnetic anisotropy contributes to the enhanced magnetomechanical effect, this work enables the quantification of the enhancement.

The magnetic assembly structures with differentiability in terms of the rotational properties could potentially streamline the process of mixing, washing, separation, and identification of multiple target analytes in a single test using a microchip.

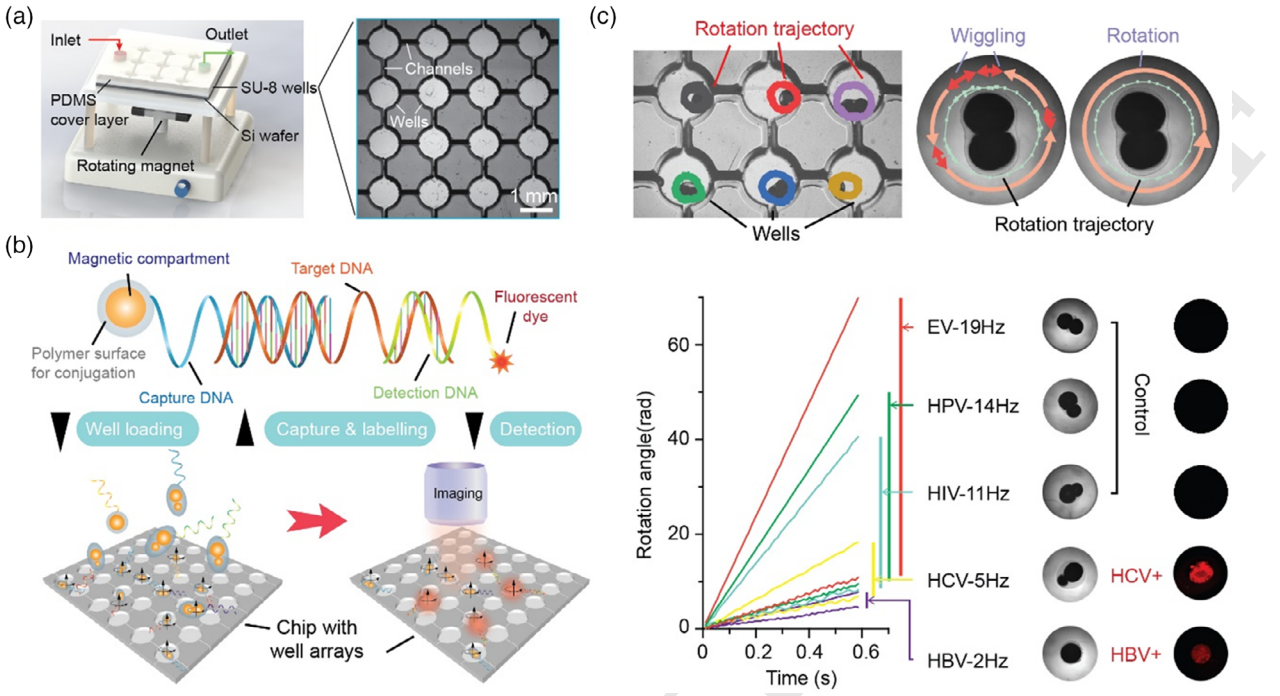

Figure 6. Dynamic assay of distinctive pathogenic DNAs based on rotation-differentiable structures. a) Microchip device accommodating swarms of structures for conducting dynamic assays, where a rotating magnet was used to regulate the frequency of magnetic field. The microchip is consisting of ~~PDMS~~ capped reaction wells fabricated on a silicon wafer. (Right) Microscopy image of the arrays of wells interconnected by flowing channels. Scale bar: 1.0 mm. b) DNA hybridization on a micromachine. The bottom row shows the workflow of dynamic DNA assays using differentiable swarms of structures. Rotation-differentiable structures are functionalized with different capture DNAs, each specific to one type of DNA targets. Groups of structures are dispersed in the patterned wells, where the sample containing target DNAs is introduced for hybridization reaction. The detection is enabled by combined fluorescent readout of the dye reporters and differentiable rotational response of the structures. c) Result of multiplexed biochemical assays for screening five different target virus DNA strands (e.g., EV, HPV, HIV, HCV, and HBV). Top panel shows structures entrapped in wells; the rotational trajectories can be extracted by motion tracking. (Bottom-left) Time-dependent rotation curves of different types of structures are plotted for rotation rate near its critical rotation frequency (±0.5 Hz). (Bottom-right) Bright field and fluorescence images of each type of structures after reactions.

The magnetorotation response, used as barcode signature, is independent to the optical domain as used in traditional suspension arrays, which suggests a promising alternative to conventional fluorescence-based approaches where the spectral crosstalk between the fluorescence encoder and reporter channels is a concern. We anticipate that the unique characteristics of dimer-type assembly structures may serve as potential building blocks to construct more complex systems, including smart sensors, actuators, and robotic devices.

4. Experimental Section

Multiphase Microfluidic Synthesis: Three syringe pumps (Microfluidic dual programmable Pump 11 Pico Plus Elite syringe pump, Harvard Apparatus) were used to drive all the fluids into a purpose-built microfluidic device (Figure S1, Supporting Information). During the generation process (Video 1, Supporting Information), the flow rate of each fluid was adjusted separately. The range of the inner flow rate was 1–100 nL s^{-1}, the middle flow rate was 1–50 nL s^{-1}, and the outer flow rate was 1–2000 nL s^{-1}, respectively. Ferrofluid nanoparticles (Ferrotec, EMG 900) with a nominal diameter of 10 nm were suspended in light hydrocarbon oil and blended with DVB with varied fractions as the inner fluid phase. An oleic acid (27728, Sigma-Aldrich) solution with 0.25% w/w Span 80 nonionic surfactant (Sigma-Aldrich) and Ca^{2+} were used as the continuous outer phase. To prepare the oil, 10 wt% $CaCl_2$ (C1016, Sigma-Aldrich) was dissolved with ethanol. Then, the same volume of ~~OA~~ was added. Finally, the solution was heated under 85 °C for 48 h. The middle phase was 2% Alginate in water containing 0.5% w/w sodium dodecyl sulfate, 0.25% w/w poly(ethylene glycol)-block-poly(propylene glycol)-block-poly(ethylene glycol) (Pluronic F108, BASF, Florham Park, NJ, USA), and 1% w/w photo-initiator (2-hydroxy-2-methylpropiophenone, 405655, Sigma-Aldrich); 15% w/w PEGDA (MW 700, 455008, Sigma-Aldrich) was used for the chemical bath of pre-matured alginate shell.

Magnetodynamic Characterization: The structures were added in the reaction wells of a micro-plate, which were placed above a magnetic stirrer with adjustable field frequencies from 1 to 35 Hz. The strength of the magnetic field provided by the setup was monitored using a three-axial Hall probe (F3A-03A02F, Senis), revealing a plateau of the in-plane dominant magnetic field across an area of 1 × 1 cm^2. For the experiments, the wells containing the structures were placed within the plateau region of the magnetic field. Videos of the rotation behaviors of the structures were taken by a high-speed camera (Andor, Zyla 4.2). The spinning curves of the structures were extracted from the video using our purpose-developed computer program allowing automatically extracting the spinning features.

Cell Culture: MCF-7 cells were used for the culture. MCF-7 cells were grown in RPMI 1640 Medium supplemented with glutamax, 10% ~~FBS~~, and antibiotics. Cells were maintained in a humidified environment with 5% CO_2 at 37 °C. The structures were pre-treated with 0.01% poly-L-lysine for 30 min under UV light and total culture medium for 15 min, and then transferred into round-bottom 96 well plates or 10 × 10 microwell

(diameter:1 mm, height: 1 mm), ready for use. Cells ~~with different concentrations (2.5×10^5, 5.0×10^5, 7.5×10^5, and 10.0×10^5 mL^{-1})~~ were seeded into round-bottom 96 well plates or microwell for 48 h ~~(original concentration of cells is 2.5×10^6 cells mL^{-1})~~. For the 3D rotation imaging, the concentration is about 2000 cells mL^{-1}. The concentration is chosen to cover the whole surface of the structures. After 48 h, the cell medium was aspirated, and the structures with cells on the surface were washed using culture medium without serum. For the staining, the PKH67 lipid dye solution was added and incubated for 5 min at room temperature. The staining solution was removed, and the structures were washed three times with complete medium.

DNA Assays: The surface of the structures was first activated with 10 mg mL^{-1} of 1-ethyl-3-(3-dimethylaminopropyl) carbodiimide (03449, Sigma-Aldrich) in 4-(2-hydroxyethyl)-1-piperazineethanesulfonic acid (HEPES) buffer (PH: 7.2, 83264, Sigma-Aldrich) for 30 min. Then, capture DNAs of 200 pmol were added in the buffer containing the structures for the reaction of 1 h. Then, the structures were washed three times with tris buffer (PH: 7.6, Tris Buffered Saline, T5030, Sigma-Aldrich). The surface of the structures was then blocked by a blocking buffer consisting of Casein (1 × TBS containing 1% Casein). For DNA hybridization, samples containing target DNAs of 200 pmol in a reaction buffer (1 × TBS containing 0.1% Casein) were added to react with the structures for 1 h. After washing the structures with tris buffer three times, fluorescent dye-labeled probe DNAs (200 pmol) in a reaction buffer were added to react with the structures. The fluorescence images of the structures were captured by a fluorescence microscope (FV1000, OLYMPUS).

Supporting Information

Supporting Information is available from the Wiley Online Library or from the author.

Acknowledgements

G.L. and Y.L. contributed equally to this work. Authors acknowledge the financial supports from the Australian Research Council (ARC) Industry Transformational Research Hub Scheme (grant IH150100028), the National Health and Medical Research Council (NHMRC) Fellowship Scheme (GNT1160635—G.L.), and the German Research Foundation (DFG) (Grant MA 5144/14-1—D. M.).

Conflict of Interest

The authors declare no conflict of interest.

Keywords

dynamic evaluation of 3D cell cultures, ~~Micromachines~~, motion trackable and differentiable, parallelized bioassay, tailorable magnetic coupling

Received: September 5, 2020
Revised: October 13, 2020
Published online:

[1] J. Zhang, J. Yan, S. Granick, *Angew. Chem., Int. Ed.* **2016**, *55*, 5166.
[2] G. M. Whitesides, B. Grzybowski, *Science* **2002**, *295*, 2418.
[3] R. Groß, M. Dorigo, *Proc. IEEE* **2008**, *96*, 1490.
[4] M. Wang, L. He, Y. Yin, *Mater. Today* **2013**, *16*, 110.
[5] M. Gao, M. Kuang, L. Li, M. Liu, L. Wang, Y. Song, *Small* **2018**, *14*, 1800117.
[6] R. Parreira, E. Özelçi, M. S. Sakar, *Adv. Intell. Syst.* **2020**, *2*, 2000062.
[7] W. Wang, J. Giltinan, S. Zakharchenko, M. Sitti, *Sci. Adv.* **2017**, *3*, e1602522.
[8] S. H. Kim, S. Y. Lee, S. M. Yang, G. R. Yi, *NPG Asia Mater.* **2011**, *3*, 25.
[9] S. N. Yin, S. Yang, C. F. Wang, S. Chen, *J. Am. Chem. Soc.* **2016**, *138*, 566.
[10] A. I. Hochbaum, R. Fan, R. He, P. Yang, *Nano Lett.* **2005**, *5*, 457.
[11] A. N. Shipway, E. Katz, I. Willner, *ChemPhysChem* **2000**, *1*, 18.
[12] R. M. Erb, H. S. Son, B. Samanta, V. M. Rotello, B. B. Yellen, *Nature* **2009**, *457*, 999.
[13] Y. Alapan, B. Yigit, O. Beker, A. F. Demirörs, M. Sitti, *Nat. Mater.* **2019**, *18*, 1244.
[14] K. Han, C. W. Shields, N. M. Diwakar, B. Bharti, G. P. López, O. D. Velev, *Sci. Adv.* **2017**, *3*, e1701108.
[15] A. Snezhko, I. S. Aranson, *Nat. Mater.* **2011**, *10*, 698.
[16] A. F. Demirörs, P. P. Pillai, B. Kowalczyk, B. A. Grzybowski, *Nature* **2013**, *503*, 99.
[17] H. Le Ferrand, S. Bolisetty, A. F. Demirörs, R. Libanori, A. R. Studart, R. Mezzenga, *Nat. Commun.* **2016**, *7*, 12078.
[18] S. Kralj, D. Makovec, *ACS Nano* **2015**, *9*, 9700.
[19] B. B. Yellen, G. Friedman, *Langmuir* **2004**, *20*, 2553.
[20] X. Liu, N. Kent, A. Ceballos, R. Streubel, Y. Jiang, Y. Chai, P. Y. Kim, J. Forth, F. Hellman, S. Shi, D. Wang, B. A. Helms, P. D. Ashby, P. Fischer, T. P. Russell, *Science* **2019**, *365*, 264.
[21] Z. Li, M. Wang, X. Zhang, D. Wang, W. Xu, Y. Yin, *Nano Lett.* **2019**, *19*, 6673.
[22] S. Sacanna, L. Rossi, D. J. Pine, *J. Am. Chem. Soc.* **2012**, *134*, 6112.
[23] J. Ge, H. Lee, L. He, J. Kim, Z. Lu, H. Kim, J. Goebl, S. Kwon, Y. Yin, *J. Am. Chem. Soc.* **2009**, *131*, 15687.
[24] J. Ge, L. He, Y. Hu, Y. Yin, *Nanoscale* **2011**, *3*, 177.
[25] L. He, M. Wang, J. Ge, Y. Yin, *Acc. Chem. Res.* **2012**, *45*, 1431.
[26] R. Dreyfus, J. Baudry, M. L. Roper, M. Fermigier, H. A. Stone, J. Bibette, *Nature* **2005**, *437*, 862.
[27] C. Wang, K. Sim, J. Chen, H. Kim, Z. Rao, Y. Li, W. Chen, J. Song, R. Verduzco, C. Yu, *Adv. Mater.* **2018**, *30*, 1706695.
[28] Y. Li, F. Mou, C. Chen, M. You, Y. Yin, L. Xu, J. Guan, *RSC Adv.* **2016**, *6*, 10697.
[29] J. M. Zhang, A. A. Aguirre-Pablo, E. Q. Li, U. Buttner, S. T. Thoroddsen, *RSC Adv.* **2016**, *6*, 81120.
[30] R. Dong, C. Wang, Q. Wang, A. Pei, X. She, Y. Zhang, Y. Cai, *Nanoscale* **2017**, *9*, 15027.
[31] S. Palagi, A. G. Mark, S. Y. Reigh, K. Melde, T. Qiu, H. Zeng, C. Parmeggiani, D. Martella, A. Sanchez-Castillo, N. Kapernaum, F. Giesselmann, D. S. Wiersma, E. Lauga, P. Fischer, *Nat. Mater.* **2016**, *15*, 647.
[32] Y. Sun, Y. Liu, B. Song, H. Zhang, R. Duan, D. Zhang, B. Dong, *Adv. Mater. Interfaces* **2019**, *6*, 1801965.
[33] B. Han, Y. L. Zhang, L. Zhu, Y. Li, Z. C. Ma, Y. Q. Liu, X. L. Zhang, X. W. Cao, Q. D. Chen, C. W. Qiu, H. B. Sun, *Adv. Mater.* **2019**, *31*, 1806386.
[34] H. Cheng, F. Zhao, J. Xue, G. Shi, L. Jiang, L. Qu, *ACS Nano* **2016**, *10*, 9529.
[35] J. G. S. Moo, C. C. Mayorga-Martinez, H. Wang, B. Khezri, W. Z. Teo, M. Pumera, *Adv. Funct. Mater.* **2017**, *27*, 1604759.
[36] S. Sánchez, L. Soler, J. Katuri, *Angew. Chem., Int. Ed.* **2015**, *54*, 1414.
[37] X. Yan, Q. Zhou, M. Vincent, Y. Deng, J. Yu, J. Xu, T. Xu, T. Tang, L. Bian, Y. X. J. Wang, K. Kostarelos, L. Zhang, *Sci. Robot.* **2017**, *2*, eaaq1155.
[38] W. Yu, H. Lin, Y. Wang, X. He, N. Chen, K. Sun, D. Lo, B. Cheng, C. Yeung, J. Tan, D. Di Carlo, S. Emaminejad, *Sci. Robot.* **2020**, *5*, eaba4411.
[39] J. Kim, S. E. Chung, S. E. Choi, H. Lee, J. Kim, S. Kwon, *Nat. Mater.* **2011**, *10*, 747.

[40] H. Yu, W. Tang, G. Mu, H. Wang, X. Chang, H. Dong, L. Qi, G. Zhang, T. Li, *Micromachines* **2018**, *9*, 540.
[41] B. Jurado-Sánchez, M. Pacheco, J. Rojo, A. Escarpa, *Angew. Chem., Int. Ed.* **2017**, *56*, 6957.
[42] Y. Zhang, L. Zhang, L. Yang, C. I. Vong, K. F. Chan, W. K. K. Wu, T. N. Y. Kwong, N. W. S. Lo, M. Ip, S. H. Wong, J. J. Y. Sung, P. W. Y. Chiu, L. Zhang, *Sci. Adv.* **2019**, *5*, eaau9650.
[43] B. Esteban-Fernández de Ávila, M. A. Lopez-Ramirez, D. F. Báez, A. Jodra, V. V. Singh, K. Kaufmann, J. Wang, *ACS Sensors* **2016**, *1*, 217.
[44] L. Soler, V. Magdanz, V. M. Fomin, S. Sanchez, O. G. Schmidt, *ACS Nano* **2013**, *7*, 9611.
[45] Q. Zhang, R. Dong, Y. Wu, W. Gao, Z. He, B. Ren, *ACS Appl. Mater. Interfaces* **2017**, *9*, 4674.
[46] B. Jurado-Sánchez, S. Sattayasamitsathit, W. Gao, L. Santos, Y. Fedorak, V. V. Singh, J. Orozco, M. Galarnyk, J. Wang, *Small* **2015**, *11*, 499.
[47] D. A. Uygun, B. Jurado-Sánchez, M. Uygun, J. Wang, *Environ. Sci. Nano* **2016**, *3*, 559.
[48] Q. Xiong, C. Y. Lim, J. Ren, J. Zhou, K. Pu, M. B. Chan-Park, H. Mao, Y. C. Lam, H. Duan, *Nat. Commun.* **2018**, *9*, 1743.
[49] S. E. Chung, X. Dong, M. Sitti, *Lab Chip* **2015**, *15*, 1667.
[50] E. Diller, *Found. Trends Robot.* **2011**, *2*, 143.
[51] F. Berndt, G. Shah, R. M. Power, J. Brugués, J. Huisken, *Nat. Commun.* **2018**, *9*, 5025.
[52] G. Lin, D. D. Karnaushenko, G. S. C. Bermúdez, O. G. Schmidt, D. Makarov, *Small* **2016**, *12*, 4553.
[53] G. Lin, D. Makarov, M. Medina-Sánchez, M. Guix, L. Baraban, G. Cuniberti, O. G. Schmidt, *Lab Chip* **2015**, *15*, 216.
[54] C. Chen, Y. Zhao, J. Wang, P. Zhu, Y. Tian, M. Xu, L. Wang, X. Huang, *Micromachines* **2018**, *9*, 160.
[55] L. Y. Chu, A. S. Utada, R. K. Shah, J. W. Kim, D. A. Weitz, *Angew. Chem., Int. Ed.* **2007**, *46*, 8970.
[56] C. P. Moerland, L. J. Van IJzendoorn, M. W. J. Prins, *Lab Chip* **2019**, *19*, 919.
[57] X. J. A. Janssen, A. J. Schellekens, K. van Ommering, L. J. Van IJzendoorn, M. W. J. Prins, *Biosens. Bioelectron.* **2009**, *24*, 1937.
[58] P. Kinnunen, *Asynchronous Magnetic Bead Rotation (AMBR) for Biosensors*, University of Michigan, Ann Arbor, MI **2011**.
[59] K. Moshksayan, N. Kashaninejad, M. E. Warkiani, J. G. Lock, H. Moghadas, B. Firoozabadi, M. S. Saidi, N.-T. Nguyen, *Sens. Actuators, B* **2018**, *263*, 151.
[60] J. Y. Park, D. H. Lee, E. J. Lee, S.-H. Lee, *Lab Chip* **2009**, *9*, 2043.
[61] G. Fang, H. Lu, A. Law, D. Gallego-Ortega, D. Jin, G. Lin, *Lab Chip* **2019**, *19*, 4093.
[62] G. Lin, M. A. B. Baker, M. Hong, D. Jin, *Chem* **2018**, *4*, 997.